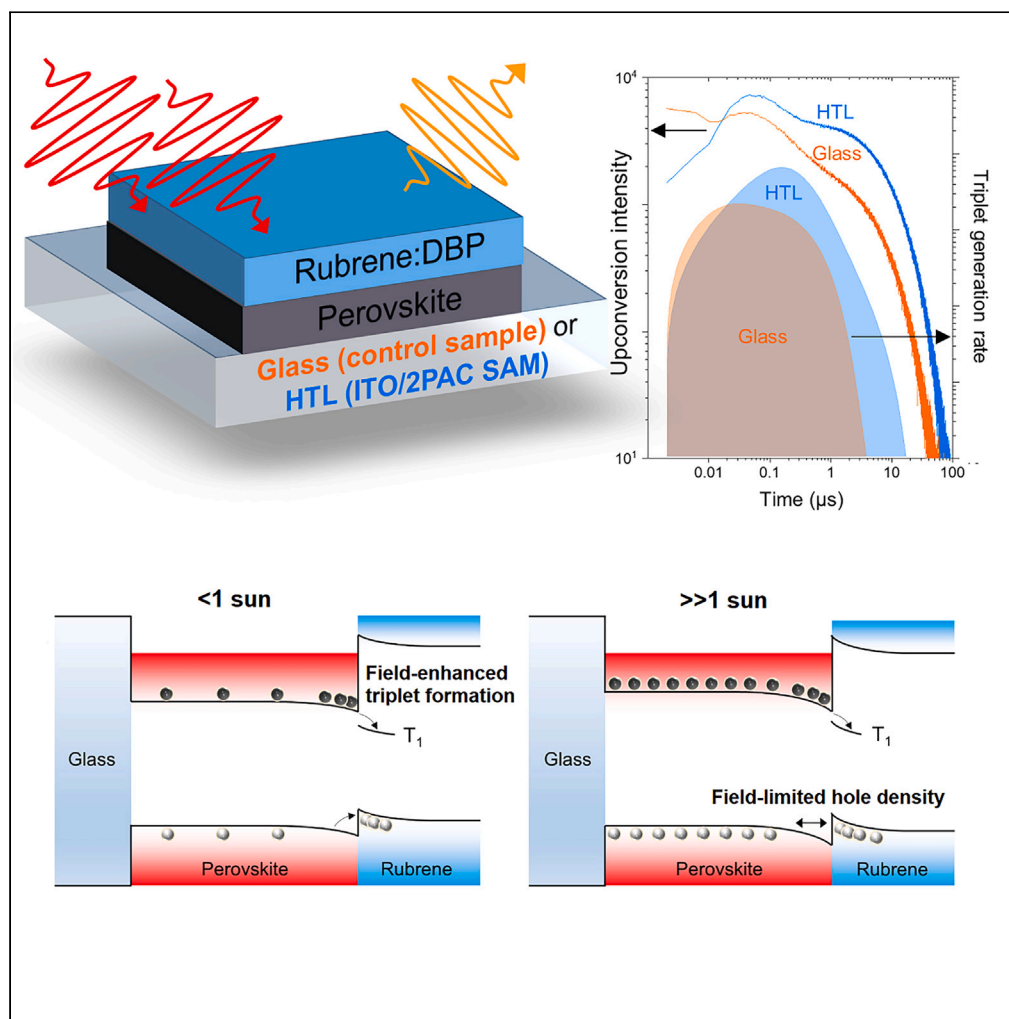**Article**

Internal electric fields control triplet formation in halide perovskite-sensitized photon upconverters

Karunanantharajah Prashanthan, Igal Levine, Artem Musiienko, ..., Martin Stolterfoht, Thomas Dittrich, Rowan W. MacQueen

rowan.macqueen@helmholtz-berlin.de

Highlights

Surface photovoltage transients revealed carrier dynamics supporting triplet formation

An internal field was altered using a hole-selective layer as the device substrate

The internal field accelerates electron-hole encounters that lead to triplet formation

Article

Internal electric fields control triplet formation in halide perovskite-sensitized photon upconverters

Karunanantharajah Prashanthan,[1,2] Igal Levine,[3] Artem Musiienko,[3] Emilio Gutierrez-Partida,[4] Hannes Hempel,[5] Klaus Lips,[1,6] Thomas Unold,[5] Martin Stolterfoht,[4] Thomas Dittrich,[3] and Rowan W. MacQueen[1,7,*]

SUMMARY

Halide perovskite-based photon upconverters utilize perovskite thin films to sensitize triplet exciton formation in a small-molecule layer, driving triplet-triplet annihilation upconversion. Despite having excellent carrier mobility, these systems suffer from inefficient triplet formation at the perovskite/annihilator interface. We studied triplet formation in formamidinium-methylammonium lead iodide/rubrene bilayers using photoluminescence and surface photovoltage methods. By studying systems constructed on glass as well as hole-selective substrates, comprising self-assembled layers of the carbazole derivative 2PACz ([2-(9H-carbazol-9-yl)ethyl]phosphonic acid) on indium-doped tin oxide, we saw how changes in the carrier dynamics induced by the hole-selective substrate perturbed triplet formation at the perovskite/rubrene interface. We propose that an internal electric field, caused by hole transfer at the perovskite/rubrene interface, strongly affects triplet exciton formation, accelerating exciton-forming electron-hole encounters at the interface but also limiting the hole density in rubrene at high excitation densities. Controlling this field is a promising path to improving triplet formation in perovskite/annihilator upconverters.

INTRODUCTION

Photon upconverters are materials that combine the energies of two or more absorbed photons through incoherent electronic processes and emit light at energies well above the optical gap of the system. Exciting a photon upconverter near its optical gap generates photoluminescence (PL) that is anti-Stokes shifted, in other words, shifted toward higher energy relative to the excitation source. This phenomenon has applications, in fields such as phototherapy,[1–3] imaging,[4] photocatalysis,[5,6] and photovoltaics.[7–9]

In photovoltaics, photon upconversion (UC) offers a means to address transmission loss in solar cells,[10] where photons that have insufficient energy to excite across a solar cell's band gap are transmitted through the solar cell rather than being absorbed. Because solar radiation approximates a black body spectrum, some portion of the available solar energy will always be subjected to transmission loss. The severity of transmission losses increase along with a solar cell's band gap.[11] An upconverter attached to the rear of a bifacial solar cell can reduce transmission loss, absorbing a portion of the transmitted low-energy light stream, upconverting it and sending back into the solar cell a higher-energy photon stream, capable of exciting across the band gap. This results in additional photocurrent being generated and hence an improved power-conversion efficiency.[12–14]

Photochemical upconverters utilize annihilators, molecular chromophores that undergo triplet-triplet exciton annihilation (TTA), sensitized by a second light-absorbing species known as the triplet sensitizer.[15] During TTA, two proximate triplet-excited annihilator molecules pool their energy, resulting in the excitation of one molecule to a state with energy approximately twice that of the initial triplet. Radiative relaxation of this molecule by an allowed transition to the ground state yields "upconverted" PL, with this overall process known as triplet-triplet annihilation UC (TTA-UC).[16–19]

[1]Department Spins in Energy Conversion and Quantum Information Science, Helmholtz-Zentrum Berlin für Materialien und Energie GmbH, 14109 Berlin, Germany

[2]Department of Physics, University of Jaffna, Jaffna, Sri Lanka

[3]Institute for Silicon Photovoltaics, Helmholtz-Zentrum Berlin für Materialien und Energie GmbH, 14109 Berlin, Germany

[4]Institute of Physics and Astronomy, University of Potsdam, Karl-Liebknecht-Str. 24–25, 14476 Potsdam-Golm, Germany

[5]Department Structure and Dynamics of Energy Materials, Helmholtz-Zentrum Berlin für Materialien und Energie GmbH, 14109 Berlin, Germany

[6]Berlin Joint EPR Laboratory, Department of Physics, Freie Universität Berlin, 14195 Berlin, Germany

[7]Lead contact
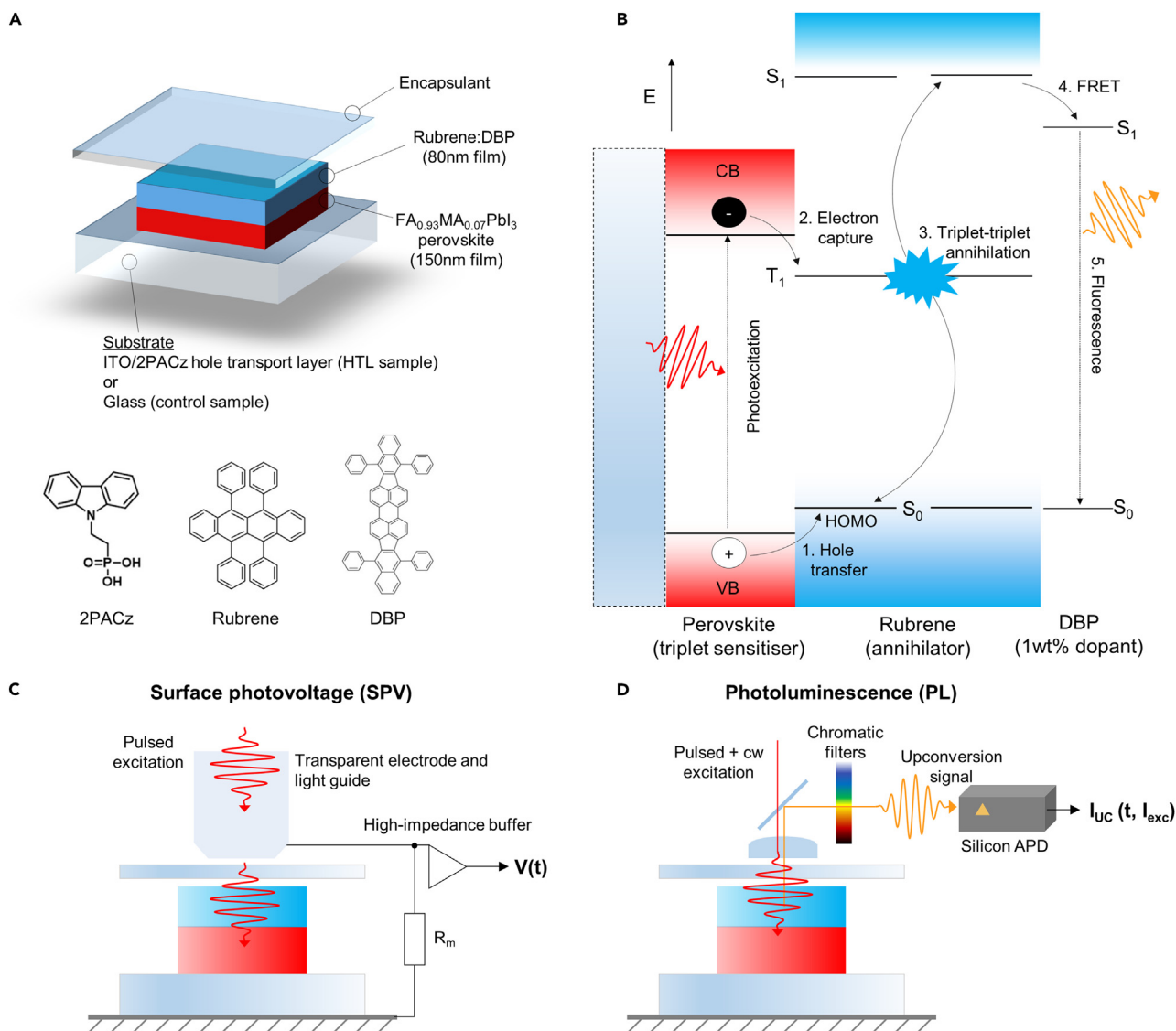
*Correspondence: rowan.macqueen@helmholtz-berlin.de

https://doi.org/10.1016/j.isci.2023.106365

Figure 1. Experimental scheme

(A) Physical structure of an upconvertering perovskite/annihilator bilayer device. The molecular structure of the HTL-forming molecule 2PACz, as well as rubrene and DBP, are drawn.

(B) Energy-level diagram of one such upconverter built on a glass substrate, depicting the processes involved in triplet formation and upconversion: carrier-driven triplet formation by sequential charge transfer at the perovskite/rubrene interface (1 and 2), triplet-triplet annihilation (3), energy transfer to DBP via Förster resonance energy transfer (FRET, 4), and finally the emission of upconverted photoluminescence (5).

(C) Diagram of the surface photovoltage measurement, in which the sample is placed within a parallel capacitor plate configuration and optically excited through a combined transparent electrode and light guide. The voltage across the capacitor plates is read out through a high-impedance buffer. R_m is a resistive load to ground that discharges the capacitor.

(D) Diagram showing the photoluminescence setup, a homebuilt confocal apparatus, which uses a beam sampler and chromatic filters to separate the excitation and photoluminescence signals.

Photochemical upconverters using halide perovskite thin films as triplet sensitizer are an emerging TTA-UC system. As shown in Figure 1B, perovskite/annihilator bilayer upconverters utilize charge carriers generated by photoexcitation of a halide perovskite thin film to generate triplet excitons in the annihilator layer.[20–22] The perovskite thin film in this system takes on the triplet sensitization role more commonly carried out by excitonic triplet sensitizers, such as organometallic complexes and lead chalcogenide nanocrystals.[23–25]

Key to this process functioning well, however, is the efficient conversion of photoinduced charge carriers in the perovskite film into triplet excitons within the annihilator layer. The current working model for this process is sequential charge transfer, depicted in Figure 1B. In this process, hole transfer from the valence band of the excited perovskite to the highest occupied molecular orbital (HOMO) of an annihilator molecule is followed by electron transfer from the perovskite conduction band to the annihilator cation, yielding a neutral annihilator molecule that is excited in the first triplet exciton state. This exciton can diffuse through the solid annihilator medium by exciton hopping and trigger TTA-UC upon encountering another triplet.

Unfortunately, all current data suggest that the yield of triplet formation at the perovskite/annihilator interface is low. First, no study to our knowledge has reported significant quenching of the perovskite sensitizer PL upon adding an annihilator layer to the surface of the film. While the annihilator layer can induce effects such as surface passivation that prolong the perovskite carrier lifetime and hence might mask a small quenching effect, consumption of a substantial proportion of carriers by triplet exciton generation must quench PL to a corresponding degree, analogous to the PL from a solar cell quenching as carriers are extracted from the device.[26]

A second argument pointing toward inefficient triplet formation is the excitation density dependence of the UC intensity. This is a measurement often used to quantify thresholds for the switch between monomolecular- and bimolecular-dominated decay processes.[27] Regimes above and below a threshold are characterized by a value of k, where k is the exponent that relates UC intensity (I_{UC}) to excitation intensity (I_{exc}) through the power law relationship $I_{UC} \propto I_{exc}^{k}$. We have observed a trend in our material and in the reports of other groups[28–30] whereby k becomes <1.0 above an excitation density of approximately 250 mW/cm^2 (equivalent to the intensity of ~2.5 suns), signifying reduced UC efficiency as the system is pumped harder. This UC efficiency roll-off is consistent with a relatively slow triplet formation process being outcompeted by perovskite radiative recombination, a process that scales with the square of carrier density and hence becomes increasingly rapid as density increases.[31] Only slow and hence inefficient triplet formation would be susceptible to this competition. The main challenge in this system is therefore to increase the efficiency of triplet formation at the perovskite/annihilator interface.

Recent work suggests that the energy-level alignment at the perovskite/annihilator interface is one crucial factor affecting triplet formation,[32] while hot carriers may also play a role.[33] In this study, we prepared perovskite/annihilator bilayers on a hole transport layer (HTL), a sample structure that we hoped would shed light on the processes limiting triplet formation by intentionally disrupting the usual carrier dynamics. Along with control samples on a normal glass substrate, we measured the charge carrier and exciton dynamics in our samples using a combination of transient surface photovoltage (SPV) and PL methods, which are depicted in Figures 1C and 1D, respectively. In transient SPV, the sample is situated within a parallel-plate capacitor and the photovoltage is read out through a high-impedance buffer following photoexcitation by a short laser pulse.[34] Because this is a non-contact method, no electrode deposition on the sample is required, nor is any electrical connection made between the sample and the SPV apparatus. SPV transients convey information on the evolution of carrier separation and diffusion, trapping, and recombination throughout the vertical height of the sample. The sign of the SPV signal indicates the spatially weighted charge distribution, allowing visualization and modeling of carrier accumulation within charge-selective layers.[35,36] Using SPV, we monitored changes in the carrier dynamics starting from a bare perovskite film on glass, then incorporating the annihilator layer and the HTL. Numerical rate modeling of the various SPV transients yielded approximate carrier density transients for each layer of a given device. These were instrumental in understanding the different effects of the HTL on the triplet formation process. We monitored triplet formation indirectly via transient and steady-state measurements of the UC PL signal.

RESULTS AND DISCUSSION

We fabricated bilayer upconverters consisting of a 50 nm rubrene film doped with 1 wt % DBP (tetraphenyldibenzoperiflanthene) deposited on a ~175 nm FA$_{0.93}$MA$_{0.07}$PbI$_3$ film (FA = formamidinium, MA = methylammonium). Film thickness, morphology, X-ray diffraction, and optical absorption data are contained in the supporting information section S1 (Figures S1–S3). We used a chloride-rich precursor approach to the perovskite film formation and annealed the layer in ambient air. We found this approach to yield highly reproducible UC performance and no short-term photoinstability in the UC intensity, a phenomenon that was termed pre-charging.[37] According to device studies, the use of a chloride-rich perovskite

precursor may induce an intermediate black α phase of FAPbI$_3$ and stabilize the perovskite crystal structure.[38] The DBP dopant in the rubrene layer increases the effective fluorescence quantum yield of the layer by acting as a fluorescent sink for singlets generated by TTA in rubrene.[39]

We prepared perovskite/annihilator bilayers on a substrate that functions as a HTL, consisting of a self-assembled monolayer of 2PACz ([2-(9H-carbazol-9-yl)ethyl]phosphonic acid), a carbazole-based moiety with a phosphonic acid linking group,[40] deposited on a 150 nm thick indium-doped tin oxide (ITO) film on glass. Such layers have been used recently as high-selectivity, low-recombination HTLs in perovskite solar cells.[40,41] Because there was no charge extraction from the device, the HTL established a hole-selective membrane effect and allowed the formation of a dynamic equilibrium between hole reservoirs in the perovskite and the ITO layers. We confirmed that the 2PACz layer remained attached to the ITO substrate during perovskite processing by preparing an identical structure on ITO but omitting the 2PACz-deposition step; this test device exhibited greatly diminished PL and UC signals and SPV transients with opposite polarity compared to the ITO/2PACz device, thus affirming the enduring effect of the 2PACz treatment.

The annihilator layer in our samples, rubrene, also functions as an HTL, so devices featuring the 2PACz HTL and rubrene layer had the structure p/i/p. The control sample consisted of the same perovskite/rubrene bilayer prepared on standard glass, which had no carrier-selective properties. In the following, the upconverter prepared on the ITO/2PACz HTL is referred to simply as the 2PACz HTL sample, and the upconverter on glass as the glass sample. Importantly, SEM measurements showed that the perovskite film thickness and surface morphology were near-identical when preparing the film on glass and 2PACz HTL substrates.

UC, perovskite PL, and SPV transients were collected with photoexcitation provided by sub-nanosecond laser pulses. Excitation intensity-dependent UC under continuous wave (cw) illumination was also collected. This body of data allowed us to link changes in the charge carrier accumulation resulting from the introduction of transport layers to changes in the triplet generation process operating at the perovskite/annihilator interface.

Transient SPV measurements

The SPV transients for two pairs of samples, based on glass and 2PACz HTL substrates, are shown in the upper pane of Figure 2. The transients were collected with a fluence of 2.6 μJ/cm^2 and corrected for baseline offset and sample capacitance. SPV transients collected at lower fluences showed no noteworthy changes in dynamics, so we report only the highest fluence transients here.

The SPV transient of bare perovskite film on glass is positive, which we assign to electron trapping at the glass/perovskite interface.[36] The addition of a rubrene layer on top of the perovskite film (glass/perovskite/rubrene structure) results in a higher positive amplitude SPV transient, consistent with hole transfer and accumulation within the rubrene layer. This result supports the sequential charge transfer mechanism of triplet formation, which requires hole transfer to the annihilator layer as the first step,[42] as well as reports of rubrene functioning as a HTL in halide perovskite solar cells.[43]

The ITO/2PACz/perovskite system exhibits a strikingly different SPV transient. After a small positive signal, which could be assigned to electron trapping at the ITO/2PACz interface,[36] the SPV turns pronouncedly negative, indicating hole accumulation in the ITO gated by the hole-selective 2PACz layer. After reaching a minimum at 350ns, the SPV signal rises again over several microseconds, reaching a small positive value after 3μs.

The ITO/2PACz/perovskite transient reveals a dynamic equilibrium forming between holes in the perovskite film and the ITO layer. Directly after photoexcitation, the large disparity in hole density within the perovskite and the ITO layer, as well as a presumably small positive driving force for hole transfer from the perovskite to the ITO (vide infra), drives the accumulation of holes within the ITO layer. At the same time, carrier recombination within the perovskite film reduces the carrier density in that layer: from a perovskite PL transient measured at the same excitation density (supporting information S4), the carrier density in the perovskite film drops by 95% over this 350ns interval, which causes a shift in the equilibrium toward hole diffusion back into the perovskite film. The interplay of this density disparity, energy-level alignment, and charging results in the gradual diffusion of charge out of the ITO/2PACz layer over the next several microseconds, followed by recombination within the perovskite film.
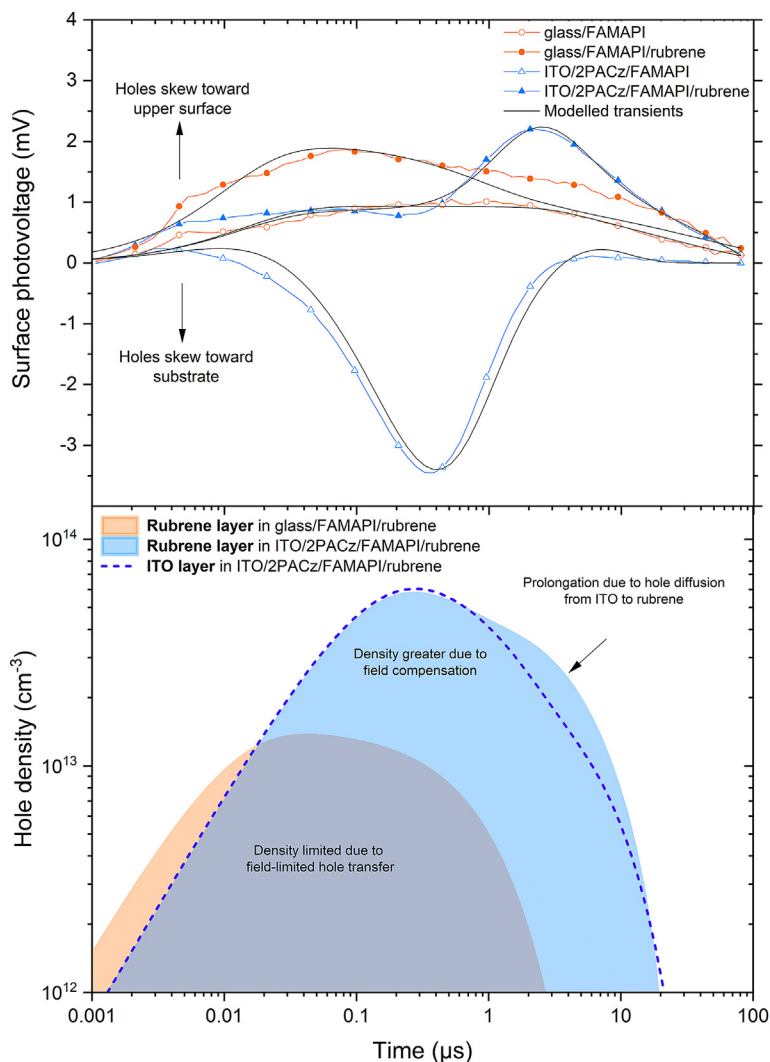
Figure 2. Surface photovoltage transients and modeling

Upper. SPV transients for the two substrate types (glass and 2PACz HTL) with and without a rubrene layer on top of the perovskite film. Polarity is as indicated: a positive SPV implies holes distributed toward the upper layer of the sample, while the polarity for electrons is opposite. Black lines indicate simulated SPV transients resulting from fitting of a carrier density model to the measured data. **Lower**. Hole density transients derived from the modeled SPV transients, for the rubrene layers of the two sample types (shaded areas) as well as for the ITO layer of the 2PACz HTL sample. The rubrene layer hole density is greater in the 2PACz HTL device due to field compensation across the device. The shoulder in the rubrene hole density transient of this device occurs as holes released from the ITO layer diffuse across the perovskite and accumulate in rubrene. The resulting disparity in charging of the 2PACz HTL and rubrene layers produces the positive spike at 2.4μs in the SPV transient.

The addition of a rubrene layer to the ITO/2PACz/perovskite structure yields the full p/i/p structure, namely ITO/2PACz/perovskite/rubrene, and hence a competition between hole transfer to the rubrene and to the 2PACz-gated ITO layer is established. The SPV transient reflects this, displaying features of both the ITO/2PACz/perovskite and the glass/perovskite/rubrene samples. The initial SPV is positive but lower in amplitude than for the glass substrate and almost constant until ∼210ns, whereupon the SPV rises in a manner reminiscent of the release of holes from ITO in the previous structure. The release time is shorter in this system—210ns compared to 350ns—which is consistent with a more rapid drop in carrier density within the perovskite film as a result of additional carrier extraction to the rubrene layer. Indeed, the perovskite PL transient for this system, measured under the same excitation conditions, indicates that the carrier density within the film again dropped by 95% when this transition point is reached (supporting information section

Table 1. Forward (K_h) and back (K_{hb}) hole transfer rates for the specified interfaces in single-heterojunction devices, derived from fitting the SPV transients with a rate model

Interface	K_h (s^{-1})	K_{hb} (s^{-1})
FAMAPI/2PACz/ITO	3.8×10^6	1.6×10^6
FAMAPI/Rubrene	4.5×10^6	3.0×10^5

S4). This result demonstrates that hole transfer between the ITO/2PACz layer and the perovskite is reversible and controlled by the carrier density in the perovskite film.

Strikingly, after ~800 ns the SPV transient of the p/i/p structure becomes more positive than that of the same perovskite/rubrene bilayer on glass, suggestive of a greater hole density in rubrene. The slow onset of this feature, occurring only after the discharge of the ITO/2PACz layer is well underway, implies that this discharge is closely connected to the increased hole density in the rubrene layer. Our interpretation of this, supported by SPV modeling (vide infra), is that holes released from the ITO/2PACz layer diffuse across the perovskite film and accumulate within the rubrene layer. By storing holes directly after photoexcitation and releasing them after the perovskite carrier density is reduced, the 2PACz HTL reduces carrier loss by radiative recombination in the perovskite and hence increases the proportion of carriers able to participate in triplet formation. Integrating over the corresponding perovskite PL transients (Figure S9) shows that the perovskite PL emitted by the HTL sample is 1.8 times lower than that of the glass sample, consistent with the extraction of holes from the perovskite film leading to a reduction in radiative recombination. However, our modeling suggests that this charge-retention function is not the only means by which the 2PACz HTL contributes to an increased rubrene hole density. To fully explain our results, we invoke sample charging and the corresponding formation of an electric field, as elucidated in the following passages.

We carried out SPV transient numerical rate modeling, extending a model previously developed to explain the carrier dynamics at buried hole-selective interfaces in perovskite solar cells.[36] The one-dimensional model generates the carrier density as a function of time at a series of fixed spatial points, each corresponding to a device layer (i.e., substrate, perovskite, or rubrene) as well as bulk and surface perovskite traps. Recombination rates and inter-layer fluxes were determined by a set of rate constants, which form the model's fitting parameters. The Adams backward differentiation formula solving algorithm was used to numerically generate the time-dependent carrier densities for each layer, from which the SPV transient was subsequently derived. Simulated SPV transients were fitted to the data using the Levenberg-Marquardt method. The SPV of the 2PACz HTL device was calculated as follows:

$$\text{SPV} = \frac{d_P}{2\varepsilon_0} \left(L_1 \frac{p_R - n_R}{\varepsilon_R} + L_2 \frac{n_{ITO} - p_{ITO}}{\varepsilon_{ITO}} + L_3 \frac{p_P - n_P - n_t}{\varepsilon_P} + L_3 \frac{n_{St}}{\varepsilon_P} \right) \qquad \text{(Equation 1)}$$

Here n_x and p_x are electron and hole densities, respectively, with the subscript x denoting perovskite (P), rubrene (R), ITO/2PACz (ITO), perovskite bulk electron traps (t), and perovskite surface electron traps (St). L_1, L_2, and L_3 are charge separation distances determined by layer thicknesses. Permittivities are denoted with ε_x (ε_0 is the vacuum permittivity), and d_P is the thickness of the perovskite layer. A full description of the various parameters, as well as their optimized values and the resulting carrier density transients, are given in the supporting information section S2 and in the STAR Methods section. Figure S4 depicts the modeled processes, while Figures S5–S8 depict the modeled carrier density transients for each layer of all of the measured devices.

The simulated SPV transients are shown overlaid with the experimental data in the upper panel of Figure 2. There is good agreement between the measured and simulated transients. In particular, the crossing points and maxima of the SPV transients are well reproduced. The rate constants for forward (K_h) and reverse (K_{hb}) hole transfer at the perovskite/2PACz/ITO and perovskite/rubrene interfaces are given in Table 1.

The model results show that hole transfer between the perovskite and the ITO/2PACz HTL is slower and more reversible compared to perovskite and rubrene, suggesting a lower driving force and hence smaller energy level offset at that interface. This is consistent with literature reports. Al-Ashouri et al. reported iso-energetic energy-level alignment (i.e., no energy level offset) for a 2PACz-based HTL and a triple-cation

halide perovskite film,[40] whereas a study of rubrene HTLs in perovskite solar cells reported an offset of approximately 100 meV for that interface.[43]

Carrier density transients for each layer of the devices were generated during the SPV transient modeling. The modeled hole density of the rubrene layer for the two upconverter device architectures is depicted in the lower panel of Figure 2, alongside the hole density in the ITO layer for the 2PACz HTL device. A surprising result is that employing the 2PACz HTL predicts a ∼4 times greater peak hole density in rubrene compared to the system based on a glass substrate. This effect is not obvious from the SPV transient alone due to the p/i/p structure leading to a near-symmetric buildup of hole density on both surfaces of the sample, thus canceling a majority of the SPV signal. But the UC PL transients and simulated triplet-formation rate, presented in the next section, clearly substantiate the model's findings.

The charge-retention function of the 2PACz HTL discussed earlier is clearly visible in the carrier density transients found in the lower panel of Figure 2. The release of holes stored in the ITO layer coincides with a knee in the corresponding rubrene hole density transient, implying the re-accumulation of these released holes in the rubrene layer after diffusing across the perovskite film. This shifts the charge distribution in the device, causing the positive growth of the SPV transient after ∼1μs.

Charge retention cannot explain all aspects of the SPV transient results, however. In the first moments after photoexcitation, the ITO and rubrene layers of the 2PACz HTL sample both accumulate holes at a similar rate. Both layers surpass the hole density of the rubrene layer in the glass device at ∼17ns, eventually reaching the previously mentioned ∼4 times greater density. Given that both samples experienced the same initial carrier density, this implies that hole accumulation in the rubrene layer is somehow impaired in the glass device. We propose that the origin of this is sample charging, caused by hole transfer from the perovskite to the rubrene layer and resulting in the formation of an electric field, which opposes further hole transfer. The 2PACz HTL device experiences lower charging and a weaker field because holes are accumulated symetrically on both surfaces of the perovskite layer. The rubrene layer in the 2PACz HTL device is thus able to support a greater hole density in response to impulsive excitation, a result that has clear implications for the triplet formation efficiency in the UC transient experiments.

UC transients

UC transients were measured for 2PACz HTL and glass sample types and are plotted in Figure 3A. The measurements were conducted with an unchanging optical setup so that the entire set of transients can be compared directly in terms of dynamics and intensity.

Focusing on the highest excitation density transients, generated with a fluence of 3.2 μJ/cm^2, we identify and then discuss key differences between the two sample types. Following pulsed excitation, the UC intensity of the glass sample peaks within the 4ns time resolution of our experiment, decays rapidly, and then climbs to a second weaker maximum at 45ns. From there the transient decays steadily following power-law dynamics, transitioning from bimolecular- to monomolecular-dominated decay dynamics at around 1μs. This is consistent with triplet exciton decay dynamics[18] and reflects a gradual reduction in local triplet exciton density due to the cessation of carrier-driven exciton generation, diffusion away from the perovskite interface, and triplet decay.

The highest excitation density UC transient for the 2PACz HTL sample exhibits three distinct differences compared to the glass sample. The initial peak within 4ns is not seen in the system. The UC intensity maximum is reached slightly later—at about 60ns—and with an intensity 1.4 times greater than the glass sample. Finally, the 2PACz HTL UC transient decays with a substantially lower rate over the time range of ∼0.25–2.5μs, giving the appearance of a plateau, before both samples revert to monomolecular UC decay with a time constant of approximately 9μs. As a result of these differences, the 2PACz HTL sample is substantially brighter than the glass sample, emitting 3.2 times more UC over the duration of the transient.

The substantial differences between the UC transients arise from a different time-dependent triplet-formation rate induced by the 2PACz HTL. Figure 3B depicts the predicted time-dependent triplet-formation rate for the two systems, calculated using $K_{TF} \propto p_r \times n_p$, where p_r and n_p are the simulated hole and electron densities in the rubrene and perovskite layers, respectively. These values were taken from the
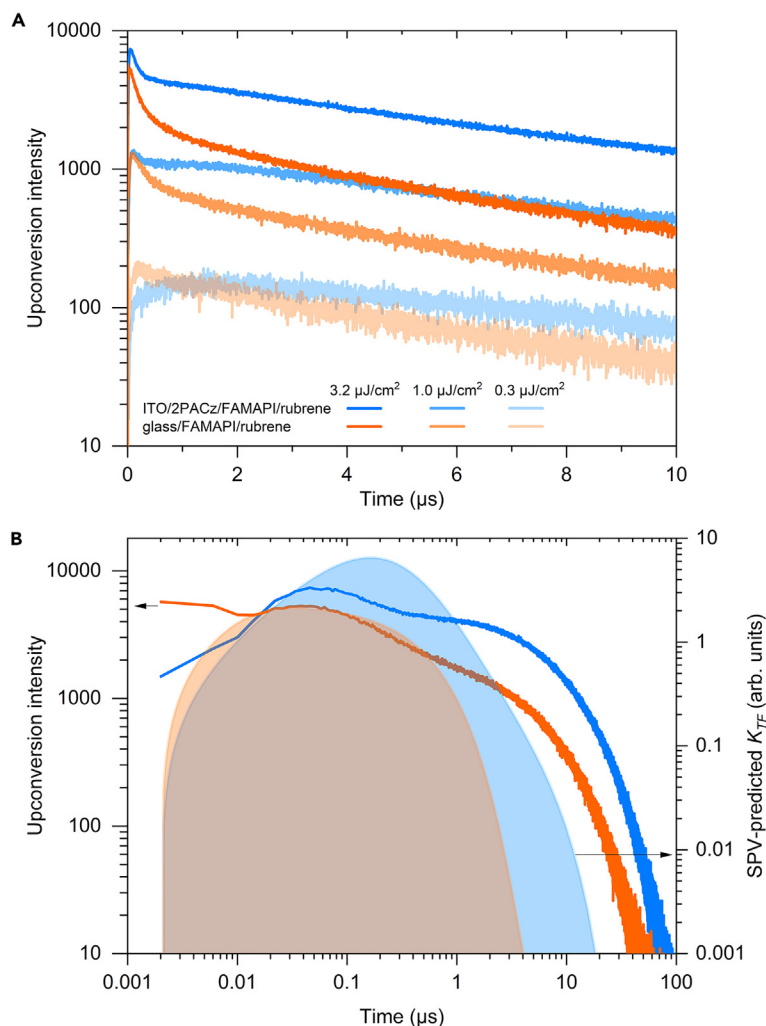
Figure 3. Upconversion PL transients and triplet-formation modeling

(A) Upconversion transients for 2PACz HTL and glass samples measured at three fluences and a 10 kHz pulse repetition rate. The transient intensities are directly comparable due to measurements being made under identical conditions.

(B) Highest-density UC transients plotted in conjunction with relative triplet-formation rates (K_{TF}) predicted from SPV transient modeling (note the double logarithmic axes). The slower onset of the UC signal and greater intensity exhibited by the 2PACz HTL sample are well correlated with the predicted triplet-formation rate. This suggests that the altered charge-carrier dynamics induced by the 2PACz HTL are responsible for the substantial changes evident in the UC dynamics.

SPV model density transients. As the rate constant for triplet formation is not known, we calculated relative rates only.

The simulated triplet formation rate transients indicate the temporal evolution of the process initiating UC, namely triplet formation, while the measured UC transients indicate the culmination of triplet formation, diffusion, and recombination via TTA. With this distinction in mind, the two sets of transients show a remarkable degree of correspondence, especially given that the triplet-formation rate transients are derived solely from SPV data. The 2PACz HTL triplet-formation rate is initially lower than that of the glass sample, like the UC transient. The crossing points of the two transient pairs are similar—16ns for the UC transients and 18ns for the triplet-formation rate transients. From then onwards, the model predicts a higher rate and longer duration of triplet formation in the HTL sample, which is in good agreement with the measured UC transients. The plateau region observed between ~0.25μs and 2.5μs in the 2PACz HTL UC transient begins

immediately after the triplet-formation rate peaks, suggesting the plateau is due to prolonged triplet generation that counteracts triplet attrition.

The origin of the different triplet-formation rates in the two systems is due to a host of effects stemming from the 2PACz HTL. As discussed previously, the 2PACz HTL improves the rubrene hole density during transient measurements through two measures: retention and delayed release of holes in the ITO layer and mitigating electric field-limited hole accumulation within rubrene. In addition, the reduction in perovskite radiative recombination as a result of accelerated carrier extraction in the p/i/p structure extends the overall carrier lifetime within the system. All three processes increase the triplet-formation yield; the first two by increasing K_{TF} directly, and the third by reducing the rate of competing radiative recombination in the perovskite layer.

The good agreement between our SPV-predicted triplet-formation rate and the UC transients suggests that a majority of triplet formation in these systems occurs slowly, utilizing thermalized rather than hot carriers.[33] This is also supported by the apparent competition between radiative recombination and triplet formation that manifests in UC efficiency roll-off. Triplet formation utilizing hot carriers should occur on the timescale of carrier cooling, namely femtoseconds to picoseconds, and hence substantially outcompetes the slower processes of inter-layer carrier diffusion and radiative recombination.[44] The susceptibility of triplet formation to these longer-timescale processes suggests that hot carriers play at most a small part in triplet formation, at least in the samples studied.

The greater hole density in the rubrene layer of the 2PACz HTL sample is not associated with any obvious indications of triplet-charge annihilation (TCA), a parasitic loss process in which triplet excitons are quenched during collisional encounters with holes in the annihilator medium.[45] We base this on the monomolecular decay times of the UC transients, which are similar for the glass and the 2PACz HTL sample types, whereas TCA would diminish this quantity in the latter sample due to the greater hole density.[30,46] While there may still be TCA effects operating on shorter timescales that are not evident without further modeling or dedicated measurement, it is clear that any enhanced TCA resulting from the greater hole density in rubrene is more than compensated by the improved triplet-formation yield.

The fluence dependence of the UC transients shown in Figure 3A is similar for the two sample types. As fluence is reduced, the risetime of the UC signal increases as a result of a slower buildup of triplet density within the annihilator layer, consistent with the result of Wieghold et al.[47] The UC intensity advantage of the 2PACz HTL sample diminishes at lower densities. This density dependence is discussed below in the context of steady-state measurements.

UC performance in the steady state

The excitation intensity response of the upconverter samples under continuous wave photoexcitation was measured, as shown in Figure 4. The measurements were conducted by recording the intensity of the UC signal while the power of a 700 nm laser beam was ramped up by translating a linear gradient neutral density filter through the beam using a motorized stage. At excitation intensities below 213 mW/cm^2, the glass sample outperforms the 2PACz HTL sample, while above it, the 2PACz HTL sample generates brighter UC. Plotted alongside the intensity data are lines indicating a power-law response with exponent k, from the expression $I_{UC} \propto I_{exc}^k$. The value of k decreases for both samples as excitation intensity is ramped up, eventually falling below 1.0, indicating diminishing UC efficiency. At the lowest intensities measured k is greater than 2.0 for the 2PACz HTL, implying that the UC process in this weak excitation regime is rate-limited by a three-body process, possibly related to charge accumulation within the two p-layers of this device.

A relative efficiency curve, also depicted in Figure 4, was generated by dividing the UC intensity by the excitation intensity. From these curves it is clear that the HTL induces a peak UC efficiency that is both greater than the glass sample and occurring at a higher excitation intensity. The UC intensity of the SAM sample asymptotically approaches 140% that of the glass control as the excitation density increases.

The crossing point of the two intensity curves corresponds to a steady-state carrier density of approximately 4×10^{15} cm^{-3}, close to the threshold at which radiative recombination becomes the dominant decay process in a prototypical halide perovskite, methylammonium lead iodide (the density calculation is shown in the supporting information S5).[48] The diminishing UC efficiency above this threshold is thus
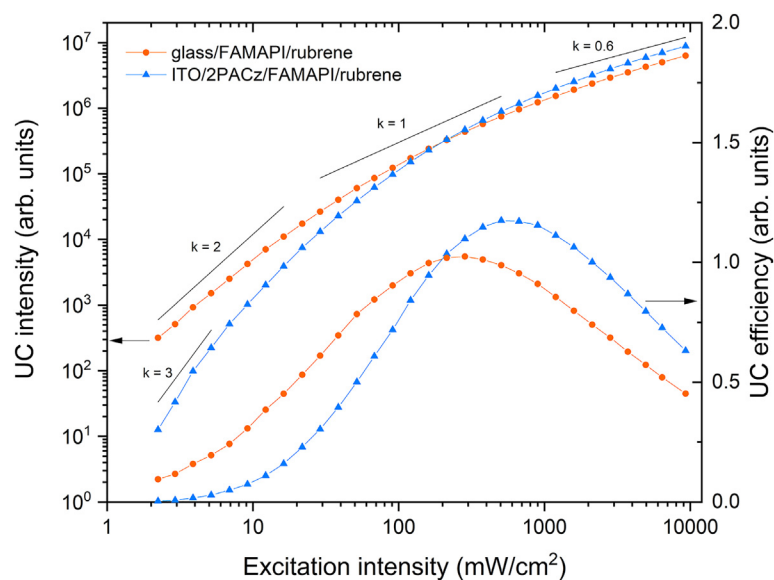
Figure 4. UC intensity and relative UC efficiency for FAMAPI/rubrene upconverters on glass (circles) and hole-selective ITO/2PACz (triangles) substrates

Lines corresponding to the indicated power-law exponent, k, are drawn as a guide to the eye. The relative UC efficiency was calculated by taking the ratio of UC intensity to excitation intensity.

likely due to the accelerating radiative recombination outcompeting triplet formation. The peak efficiency of the 2PACz HTL sample occurs at twice the excitation intensity of the glass sample, which suggests that triplet formation occurs more rapidly in this sample at high excitation densities, thus remaining more competitive with radiative recombination. Below the 213 mW/cm² crossover point, the triplet-formation efficiency becomes greater in the glass substrate sample.

Because these measurements were made under quasi-steady-state conditions, unlike the transient measurements, we cannot invoke hole retention and then release from within the ITO to explain the different UC intensity responses depicted in Figure 4. The retention and release process relies upon a nonequilibrium distribution of charge carriers existing within the device, for example, following short laser pulse excitation, whereas in quasi-steady-state conditions no net charge flow between layers takes place and the carrier distribution is essentially static. Hole extraction to the ITO layer will still result in a small surplus of electrons existing in the perovskite bulk, which may make a positive contribution to triplet generation. However, we attribute the differences in the UC intensity dependence of the two sample types largely to electric-field effects, specifically the effects of the electric field on triplet formation and on rubrene hole density. These are elucidated in the following section.

Electric field effects in carrier-driven triplet formation

A concise explanation for the different observations made in this study is the presence of an electric field at the perovskite/rubrene interface, which strongly affects the triplet formation rate. The field is generated by hole transfer from the perovskite valence band to the rubrene HOMO, which leaves the rubrene and perovskite layers positively and negatively charged, respectively. Crucially, in the 2PACz HTL sample, carriers in the perovskite experience a weaker field because holes accumulate on either side of the perovskite layer and so the device charging is balanced. This fact allowed us to measure the effects of the electric field by its (at least partial) negation in the 2PACz HTL sample.

As illustrated in Figure 5, one effect of the field is to increase carrier density in the vicinity of the perovskite/rubrene interface as carriers move in response to the field according to Coulomb's law. This increased local carrier density has been linked to nonlinearly accelerated interfacial recombination at perovskite/organic heterojunctions,[49] a process in which a pair of carriers situated on either side of the interface recombine via a surface state. Carrier-driven triplet formation is mechanistically analogous to interfacial recombination
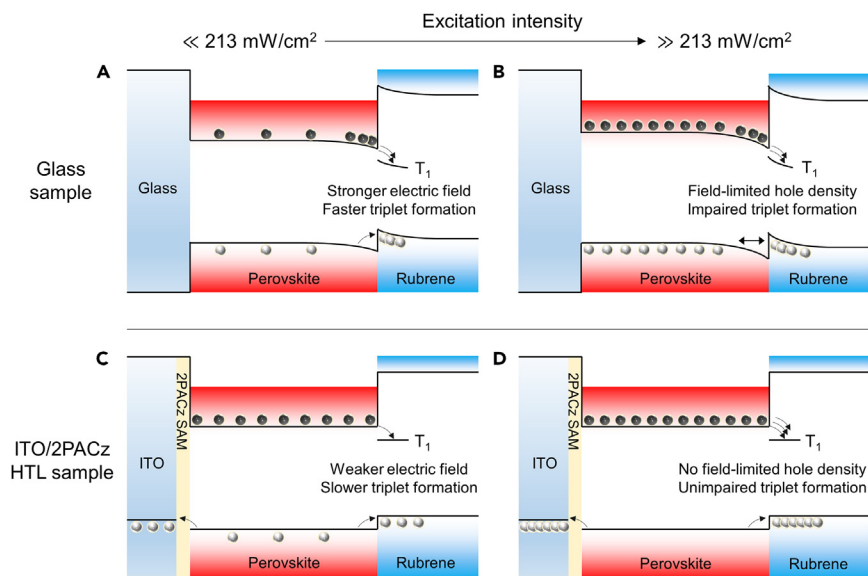
Figure 5. Electric field effects under steady-state photoexcitation

(A–D) A glass/FAMAPI/rubrene device (a and b) and a ITO/2PACz/FAMAPI/rubrene device (c and d) are depicted showing illustrative carrier accumulation, field generation, and triplet formation during exposure to high and low steady-state excitation intensities. An electric field, formed by hole transfer at the perovskite/rubrene interface, improves triplet formation by increasing the rate of electron-hole encounters at the interface. In the 2PACz HTL sample, hole transfer also occurs between the perovskite and the ITO/2PACz substrate, leading to balanced charging and diminishing the internal field. Triplet formation is correspondingly slower. However, at high excitation densities the electric field self-limits the rubrene hole density, reducing the triplet-formation yield, while the rubrene hole density in the HTL system is not field limited. The triplet-formation yield is thus greater in the HTL sample. The excitation density threshold for the changeover between these characteristics was 213 mW/cm^2.

except that it yields as the final state a triplet exciton in the annihilator. Hence a field-induced locally elevated carrier density at the perovksite/rubrene interface should likewise accelerate triplet formation.

A field-accelerated triplet-formation process is consistent with our observations. In the 2PACz HTL sample, the triplet formation rate should be less impacted by carriers bunching near the perovskite/rubrene interface since the internal field is weaker. This would result in a lower triplet formation rate relative to the glass sample when the rubrene hole density is not saturated (vide infra). Indeed, as we see in Figure 4, at low excitation intensities, the UC intensity and hence the triplet-formation efficiency in the glass sample is substantially greater than that of the 2PACz HTL.

A second effect of the hole transfer-induced electric field is self-limiting hole density within the rubrene layer. As holes transfer to rubrene, the electric field grows, opposing further hole transfer by reducing the driving force experienced by holes crossing the interface. The hole density in rubrene saturates once the electric field fully counteracts the perovskite/rubrene energy level offset that initially drove hole transfer.

Saturating rubrene hole density causes the rate of triplet formation to deteriorate relative to the photoexcitation rate since the triplet formation rate is linearly dependent on the rubrene hole density. The weaker internal field of the 2PACz HTL sample means that hole transfer to rubrene is less prone to saturation in this system, as was seen in the transient SPV measurements. As a result, the triplet-formation rate in the 2PACz HTL sample can surpass that of the glass sample once the rubrene hole density in the glass sample has saturated. This is consistent with the greater peak UC efficiency of the 2PACz HTL sample observed at high excitation intensities.

Conclusions and outlook

Despite exhibiting no net improvement in UC efficiency at ~1-sun intensities, the 2PACz HTL sample is an illuminating device architecture. In pulsed measurements at high fluence, the 2PACz HTL exhibited a

greater rubrene hole density compared to the control device and a larger UC intensity, which we attributed to improved triplet formation efficiency. At lower fluences and at circa-1 sun steady-state excitation, the 2PACz HTL diminished the UC intensity substantially. We proposed that these observations can be explained concisely by the existence of an internal electric field within the device, generated by hole transfer at the perovskite/annihilator interface. This field locally enhances the perovskite film's electron density in the vicinity of the interface, increasing the electron-transfer rate during sequential charge transfer triplet formation. On the other hand, at high excitation densities, the field imposes a limit on the density of holes that can reside in the rubrene layer before drift and diffusion influences fully counteract one another. Both of these field effects—triplet formation enhancement and hole density saturation—were less severe in the 2PACz HTL device because symmetrical hole accumulation in the p/i/p structure diminished this internal field. The comparison between glass and 2PACz HTL samples and the measurement of carrier dynamics using SPV were instrumental in making this phenomenon clear.

This findings suggest a new handle with which to engineer the performance of perovskite/annihilator up-converters, fine-tuning the energy-level alignment at the perovskite/annihilator interface to control field effects and triplet formation at a given excitation density. The give-and-take nature of the electric field effect—helping but also hindering triplet formation under different circumstances—means that targeting a specific excitation profile dictated by application may be important when considering the best approach.

A wealth of strategies exist with which to directly and indirectly alter the energy-level alignment at semiconductor heterointerfaces, including doping by solvent processing[50] and many other methods.[51] Many of these could be applied to the perovskite/annihilator system, thereby altering field effects, triplet formation, and ultimately the UC performance itself. Employing these approaches, alone or in combination with carrier-selective substrates, may be a useful strategy for improving the triplet-formation efficiency of perovskite/annihilator upconverters, unlocking new possibilities for photovoltaics and other applications.

Limitations of the study

While transient SPV measurements and modeling used in concert with time-resolved PL provided useful insight into the carrier dynamics in this study, we were unable to carry out equivalent measurements of the SPV in steady-state illumination conditions. These measurements may have provided equally useful insights into the role of the 2PACz HTL operating in steady-state conditions, strengthening the electric field-controlled model of triplet formation. We are actively developing the steady-state SPV+PL technique and will utilize this in subsequent studies.

STAR★METHODS

Detailed methods are provided in the online version of this paper and include the following:

- KEY RESOURCES TABLE
- RESOURCE AVAILABILITY
  - Lead contact
  - Materials availability
  - Data and code availability
- METHOD DETAILS
  - Substrate preparation
  - 2Pacz SAM HTL deposition on ITO
  - Perovskite film preparation
  - Rubrene:DBP film deposition and sample encapsulation
  - Film thickness, morphology and absorption measurements
  - Photoluminescence measurements
  - Surface photovoltage measurements
  - Surface photovoltage transient modelling
  - Steady-state carrier density calculation

SUPPLEMENTAL INFORMATION

Supplemental information can be found online at https://doi.org/10.1016/j.isci.2023.106365.

ACKNOWLEDGMENTS

AUTHOR CONTRIBUTIONS

This study was conceived and planned by RWM and KP, with input from IL, TU, TD, and KL. KP carried out sample preparation and photoluminescence measurements. KP, IL, HH, and RWM carried out SPV meaurements. AM performed SPV modeling. KP, EG-P, and MS developed perovskite synthesis procedures. Data processing and analysis were carried out by KP, RWM, IL, AM, and TD. RWM was the principal author and project coordinator. All authors contributed to and commented on the manuscript.

DECLARATION OF INTERESTS

The authors declare no competing interests.

REFERENCES

1. Feng, L., He, F., Liu, B., Yang, G., Gai, S., Yang, P., Li, C., Dai, Y., Lv, R., and Lin, J. (2016). g-C3N4 coated upconversion nanoparticles for 808 nm near-infrared light triggered phototherapy and multiple imaging. Chem. Mater. 28, 7935–7946. https://doi.org/10.1021/acs.chemmater.6b03598.

2. Askes, S.H.C., Bahreman, A., and Bonnet, S. (2014). Activation of a photodissociative ruthenium complex by triplet-triplet annihilation upconversion in liposomes. Angew. Chem. Int. Ed. Engl. 53, 1029–1033. https://doi.org/10.1002/anie.201309389.

3. Askes, S.H.C., Kloz, M., Bruylants, G., Kennis, J.T.M., and Bonnet, S. (2015). Triplet-triplet annihilation upconversion followed by FRET for the red light activation of a photodissociative ruthenium complex in liposomes. Phys. Chem. Chem. Phys. 17, 27380–27390. https://doi.org/10.1039/C5CP04352B.

4. Zhou, J., Liu, Z., and Li, F. (2012). Upconversion nanophosphors for small-animal imaging. Chem. Soc. Rev. 41, 1323–1349. https://doi.org/10.1039/C1CS15187H.

5. Ravetz, B.D., Pun, A.B., Churchill, E.M., Congreve, D.N., Rovis, T., and Campos, L.M. (2019). Photoredox catalysis using infrared light via triplet fusion upconversion. Nature 565, 343–346. https://doi.org/10.1038/s41586-018-0835-2.

6. Yu, T., Liu, Y., Zeng, Y., Chen, J., Yang, G., and Li, Y. (2019). Triplet–triplet annihilation upconversion for photocatalytic hydrogen evolution. Chemistry 25, 16270–16276. https://doi.org/10.1002/chem.201904025.

7. de Wild, J., Meijerink, A., Rath, J.K., van Sark, W.G.J.H.M., and Schropp, R.E.I. (2011). Upconverter solar cells: materials and applications. Energy Environ. Sci. 4, 4835–4848. https://doi.org/10.1039/C1EE01659H.

8. Richards, B.S., Hudry, D., Busko, D., Turshatov, A., and Howard, I.A. (2021). Photon upconversion for photovoltaics and photocatalysis: a critical review. Chem. Rev. 121, 9165–9195. https://doi.org/10.1021/acs.chemrev.1c00034.

9. Schulze, T.F., and Schmidt, T.W. (2015). Photochemical upconversion: present status and prospects for its application to solar energy conversion. Energy Environ. Sci. 8, 103–125. https://doi.org/10.1039/C4EE02481H.

10. Shalav, A., Richards, B.S., and Green, M.A. (2007). Luminescent layers for enhanced silicon solar cell performance: up-conversion. Sol. Energy Mater. Sol. Cell. 91, 829–842. https://doi.org/10.1016/j.solmat.2007.02.007.

11. Hirst, L.C., and Ekins-Daukes, N.J. (2011). Fundamental losses in solar cells. Prog. Photovolt:. Res. Appl. 19, 286–293. https://doi.org/10.1002/pip.1024.

12. Cheng, Y.Y., Fückel, B., MacQueen, R.W., Khoury, T., Clady, R.G.C.R., Schulze, T.F., Ekins-Daukes, N.J., Crossley, M.J., Stannowski, B., Lips, K., and Schmidt, T.W. (2012). Improving the light-harvesting of amorphous silicon solar cells with photochemical upconversion. Energy Environ. Sci. 5, 6953–6959. https://doi.org/10.1039/C2EE21136J.

13. Cheng, Y.Y., Nattestad, A., Schulze, T.F., MacQueen, R.W., Fückel, B., Lips, K., Wallace, G.G., Khoury, T., Crossley, M.J., and Schmidt, T.W. (2016). Increased upconversion performance for thin film solar cells: a trimolecular composition. Chem. Sci. 7, 559–568. https://doi.org/10.1039/C5SC03215F.

14. Singh, R., Madirov, E., Busko, D., Hossain, I.M., Konyushkin, V.A., Nakladov, A.N., Kuznetsov, S.V., Farooq, A., Gharibzadeh, S., Paetzold, U.W., et al. (2021). Harvesting sub-bandgap photons via upconversion for

perovskite solar cells. ACS Appl. Mater. Interfaces 13, 54874–54883. https://doi.org/10.1021/acsami.1c13477.

15. Singh-Rachford, T.N., and Castellano, F.N. (2010). Triplet sensitized red-to-blue photon upconversion. J. Phys. Chem. Lett. 1, 195–200. https://doi.org/10.1021/jz900170m.

16. Bharmoria, P., Bildirir, H., and Moth-Poulsen, K. (2020). Triplet–triplet annihilation based near infrared to visible molecular photon upconversion. Chem. Soc. Rev. 49, 6529–6554. https://doi.org/10.1039/D0CS00257G.

17. Gray, V., Moth-Poulsen, K., Albinsson, B., and Abrahamsson, M. (2018). Towards efficient solid-state triplet–triplet annihilation based photon upconversion: supramolecular, macromolecular and self-assembled systems. Coord. Chem. Rev. 362, 54–71. https://doi.org/10.1016/j.ccr.2018.02.011.

18. Schmidt, T.W., and Castellano, F.N. (2014). Photochemical upconversion: the primacy of kinetics. J. Phys. Chem. Lett. 5, 4062–4072. https://doi.org/10.1021/jz501799m.

19. Alves, J., Feng, J., Nienhaus, L., and Schmidt, T.W. (2022). Challenges, progress and prospects in solid state triplet fusion upconversion. J. Mater. Chem. C Mater. 10, 7783–7798. https://doi.org/10.1039/D1TC05659J.

20. Wieghold, S., Bieber, A.S., VanOrman, Z.A., Daley, L., Leger, M., Correa-Baena, J.-P., and Nienhaus, L. (2019). Triplet sensitization by lead halide perovskite thin films for efficient solid-state photon upconversion at subsolar fluxes. Matter 1, 705–719. https://doi.org/10.1016/j.matt.2019.05.026.

21. VanOrman, Z.A., and Nienhaus, L. (2021). Bulk metal halide perovskites as triplet sensitizers: taking charge of upconversion. ACS Energy Lett. 6, 3686–3694. https://doi.org/10.1021/acsenergylett.1c01794.

22. VanOrman, Z.A., Drozdick, H.K., Wieghold, S., and Nienhaus, L. (2021). Bulk halide perovskites as triplet sensitizers: progress and prospects in photon upconversion. J. Mater. Chem. C Mater. 9, 2685–2694. https://doi.org/10.1039/D1TC00245G.

23. Yanai, N., Kozue, M., Amemori, S., Kabe, R., Adachi, C., and Kimizuka, N. (2016). Increased vis-to-UV upconversion performance by energy level matching between a TADF donor and high triplet energy acceptors. J. Mater. Chem. C Mater. 4, 6447–6451. https://doi.org/10.1039/C6TC01816E.

24. Garakyaraghi, S., and Castellano, F.N. (2018). Nanocrystals for triplet sensitization: molecular behavior from quantum-confined materials. Inorg. Chem. 57, 2351–2359. https://doi.org/10.1021/acs.inorgchem.7b03219.

25. Yanai, N., and Kimizuka, N. (2017). New triplet sensitization routes for photon upconversion: thermally activated delayed fluorescence molecules, inorganic nanocrystals, and singlet-to-triplet absorption. Acc. Chem. Res.

50, 2487–2495. https://doi.org/10.1021/acs.accounts.7b00235.

26. Stolterfoht, M., Le Corre, V.M., Feuerstein, M., Caprioglio, P., Koster, L.J.A., and Neher, D. (2019). Voltage-dependent photoluminescence and how it correlates with the fill factor and open-circuit voltage in perovskite solar cells. ACS Energy Lett. 4, 2887–2892. https://doi.org/10.1021/acsenergylett.9b02262.

27. Monguzzi, A., Tubino, R., Hoseinkhani, S., Campione, M., and Meinardi, F. (2012). Low power, non-coherent sensitized photon up-conversion: modelling and perspectives. Phys. Chem. Chem. Phys. 14, 4322–4332. https://doi.org/10.1039/c2cp23900k.

28. Wieghold, S., Bieber, A.S., VanOrman, Z.A., Rodriguez, A., and Nienhaus, L. (2020). Is disorder beneficial in perovskite-sensitized solid-state upconversion? The role of DBP doping in rubrene. J. Phys. Chem. C 124, 18132–18140. https://doi.org/10.1021/acs.jpcc.0c05290.

29. Prashanthan, K., Naydenov, B., Lips, K., Unger, E., and MacQueen, R.W. (2020). Interdependence of photon upconversion performance and antisolvent processing in thin-film halide perovskite-sensitized triplet–triplet annihilators. J. Chem. Phys. 153, 164711. https://doi.org/10.1063/5.0026564.

30. Wang, L., Yoo, J.J., Lin, T.-A., Perkinson, C.F., Lu, Y., Baldo, M.A., and Bawendi, M.G. (2021). Interfacial trap-assisted triplet generation in lead halide perovskite sensitized solid-state upconversion. Adv. Mater. 33, 2100854. https://doi.org/10.1002/adma.202100854.

31. Kirchartz, T., Márquez, J.A., Stolterfoht, M., and Unold, T. (2020). Photoluminescence-based characterization of halide perovskites for photovoltaics. Adv. Energy Mater. 10, 1904134. https://doi.org/10.1002/aenm.201904134.

32. Bieber, A.S., VanOrman, Z.A., Drozdick, H.K., Weiss, R., Wieghold, S., and Nienhaus, L. (2021). Mixed halide bulk perovskite triplet sensitizers: interplay between band alignment, mid-gap traps, and phonons. J. Chem. Phys. 155, 234706. https://doi.org/10.1063/5.0077439.

33. Conti, C.R., Bieber, A.S., VanOrman, Z.A., Moller, G., Wieghold, S., Schaller, R.D., Strouse, G.F., and Nienhaus, L. (2022). Ultrafast triplet generation at the lead halide perovskite/rubrene interface. ACS Energy Lett. 7, 617–623. https://doi.org/10.1021/acsenergylett.1c02732.

34. Dittrich, T., Bönisch, S., Zabel, P., and Dube, S. (2008). High precision differential measurement of surface photovoltage transients on ultrathin CdS layers. Rev. Sci. Instrum. 79, 113903. https://doi.org/10.1063/1.3020757.

35. Fengler, S., Kriegel, H., Schieda, M., Gutzmann, H., Klassen, T., Wollgarten, M., and Dittrich, T. (2020). Charge transfer in c-Si(n++)/TiO2(ALD) at the amorphous/anatase transition: a transient surface

photovoltage spectroscopy study. ACS Appl. Mater. Interfaces 12, 3140–3149. https://doi.org/10.1021/acsami.9b17592.

36. Levine, I., Al-Ashouri, A., Musiienko, A., Hempel, H., Magomedov, A., Drevilkauskaite, A., Getautis, V., Menzel, D., Hinrichs, K., Unold, T., et al. (2021). Charge transfer rates and electron trapping at buried interfaces of perovskite solar cells. Joule 5, 2915–2933. https://doi.org/10.1016/j.joule.2021.07.016.

37. Wieghold, S., and Nienhaus, L. (2020). Precharging photon upconversion: interfacial interactions in solution-processed perovskite upconversion devices. J. Phys. Chem. Lett. 11, 601–607. https://doi.org/10.1021/acs.jpclett.9b03596.

38. Kim, M., Kim, G.-H., Lee, T.K., Choi, I.W., Choi, H.W., Jo, Y., Yoon, Y.J., Kim, J.W., Lee, J., Huh, D., et al. (2019). Methylammonium chloride induces intermediate phase stabilization for efficient perovskite solar cells. Joule 3, 2179–2192. https://doi.org/10.1016/j.joule.2019.06.014.

39. Wu, M., Congreve, D.N., Wilson, M.W.B., Jean, J., Geva, N., Welborn, M., Van Voorhis, T., Bulović, V., Bawendi, M.G., and Baldo, M.A. (2016). Solid-state infrared-to-visible upconversion sensitized by colloidal nanocrystals. Nat. Photonics 10, 31–34. https://doi.org/10.1038/nphoton.2015.226.

40. Al-Ashouri, A., Magomedov, A., Roß, M., Jošt, M., Talaikis, M., Chistiakova, G., Bertram, T., Márquez, J.A., Köhnen, E., Kasparavičius, E., et al. (2019). Conformal monolayer contacts with lossless interfaces for perovskite single junction and monolithic tandem solar cells. Energy Environ. Sci. 12, 3356–3369. https://doi.org/10.1039/C9EE02268F.

41. Al-Ashouri, A., Köhnen, E., Li, B., Magomedov, A., Hempel, H., Caprioglio, P., Márquez, J.A., Morales Vilches, A.B., Kasparavicius, E., Smith, J.A., et al. (2020). Monolithic perovskite/silicon tandem solar cell with >29% efficiency by enhanced hole extraction. Science 370, 1300–1309. https://doi.org/10.1126/science.abd4016.

42. Nienhaus, L., Correa-Baena, J.-P., Wieghold, S., Einzinger, M., Lin, T.-A., Shulenberger, K.E., Klein, N.D., Wu, M., Bulović, V., Buonassisi, T., et al. (2019). Triplet-sensitization by lead halide perovskite thin films for near-infrared-to-visible upconversion. ACS Energy Lett. 4, 888–895. https://doi.org/10.1021/acsenergylett.9b00283.

43. Ji, G., Zheng, G., Zhao, B., Song, F., Zhang, X., Shen, K., Yang, Y., Xiong, Y., Gao, X., Cao, L., and Qi, D.C. (2017). Interfacial electronic structures revealed at the rubrene/CH3NH3PbI3 interface. Phys. Chem. Chem. Phys. 19, 6546–6553. https://doi.org/10.1039/c6cp07592d.

44. Lim, H., Kwon, H., Kim, S.K., and Kim, J.W. (2017). Delayed triplet-state formation through hybrid charge transfer exciton at copper phthalocyanine/GaAs

heterojunction. J. Phys. Chem. Lett. *8*, 4763–4768. https://doi.org/10.1021/acs.jpclett.7b02111.

45. Köhler, A., and Bässler, H. (2009). Triplet states in organic semiconductors. Mater. Sci. Eng. R Rep. *66*, 71–109. https://doi.org/10.1016/j.mser.2009.09.001.

46. Thompson, N.J., Hontz, E., Congreve, D.N., Bahlke, M.E., Reineke, S., Van Voorhis, T., and Baldo, M.A. (2014). Nanostructured singlet fission photovoltaics subject to triplet-charge annihilation. Adv. Mater. *26*, 1366–1371. https://doi.org/10.1002/adma.201304588.

47. Wieghold, S., Bieber, A.S., Lackner, J., Nienhaus, K., Nienhaus, G.U., and Nienhaus, L. (2020). One-step fabrication of perovskite-based upconversion devices. ChemPhotoChem *4*, 704–712. https://doi.org/10.1002/cptc.202000068.

48. Stranks, S.D. (2017). Nonradiative losses in metal halide perovskites. ACS Energy Lett. *2*, 1515–1525. https://doi.org/10.1021/acsenergylett.7b00239.

49. Krogmeier, B., Staub, F., Grabowski, D., Rau, U., and Kirchartz, T. (2018). Quantitative analysis of the transient photoluminescence of CH3NH3PbI3/PC61BM heterojunctions by numerical simulations. Sustain. Energy Fuels *2*, 1027–1034. https://doi.org/10.1039/c7se00603a.

50. Sullivan, C.M., Bieber, A.S., Drozdick, H.K., Moller, G., Kuszynski, J.E., VanOrman, Z.A., Wieghold, S., Strouse, G.F., and Nienhaus, L. (2023). Surface doping boosts triplet generation yield in perovskite-sensitized upconversion. Adv. Opt. Mater. *11*, 2201921. https://doi.org/10.1002/adom.202201921.

51. Niederhausen, J., Mazzio, K.A., and MacQueen, R.W. (2021). Inorganic–organic interfaces in hybrid solar cells. Electron. Struct. *3*, 033002. https://doi.org/10.1088/2516-1075/ac23a3.

STAR★METHODS

KEY RESOURCES TABLE

REAGENT or RESOURCE	SOURCE	IDENTIFIER
Chemicals, peptides, and recombinant proteins		
[2-(9H-carbazol-9-yl)ethyl]phosphonic acid (2PACz)	Tokyo Chemical Industry	Prod. number C3663
Formamidinium iodide (FAI)	Dyenamo	Prod. number DN-P10-4N
Methylammonium iodide (MAI)	Dyenamo	Prod. number DN-P02-4N
Methylammonium chloride (MACl)	Dyenamo	Prod. number DN-P08-4N
Lead iodide (PbI)	Tokyo Chemical Industry	Prod. number: L0279

RESOURCE AVAILABILITY

Lead contact

Further information and requests for resources and reagents should be directed to and will be fulfilled by the lead contact, Rowan MacQueen (rowan.macqueen@helmholtz-berlin.de).

Materials availability

This study did not generate new unique reagents.

Data and code availability

- The data supporting this study is available from the authors and can be provided upon request.

- This paper does not report original code.

- Any additional information required to reanalyze the data reported in this paper is available from the lead contact upon request.

METHOD DETAILS

Substrate preparation

Glass (25 × 25 mm, VWR) and ITO (25 × 25 mm, resistivity = 15 Ω/sq, Automatic Research) substrates were cleaned sequentially in 2% Mucasol water, deionized water, acetone and isopropanol at ∼ 40°C in an ultrasonic bath for 15 min each, followed by drying under a nitrogen stream. The substrates were UV-ozone treated for 15 min.

2Pacz SAM HTL deposition on ITO

The 2PACz ([2-(9H-carbazol-9-yl)ethyl]phosphonic acid) SAM powder (Tokyo Chemical Industry) was dissolved in anhydrous ethanol at a concentration of 3 mM and ultrasonicated for at least 15 minutes at 30–40°C. A 100 μL aliquot was steadily released onto the middle of the ITO substrate and the spin-coating program (30 s at 3000 rpm) was started after closing the lid of the spin coater and leaving after ∼5 s. At the end, the substrates were annealed at 100°C for 5 minutes.

Perovskite film preparation

The perovskite precursor solution was prepared by dissolving FAI, MAI (1.2 M, 99% Dyenamo), MACl (1.2 M, 99% Dyenamo) and PbI$_2$ (1.2 M, 99.99% Tokyo Chemical Industry) in a 0.93:0.07:0.3:1.1 molar ratio in a mixed solvent ratio 4:1 of DMF (Sigma Aldrich, anhydrous, 99.8%) and DMSO (Sigma Aldrich, anhydrous, 99.9%) and diluted two-fold. A 100 μL aliquot of precursor solution was spin coated using a two-step spin coating program, 1000 rpm for 10 sec with a ramp up of 3 sec and 4000 rpm for 30 sec with a ramp up of 2 sec. During the second step, 250μL of chlorobenzene (Sigma Aldrich, anhydrous, 99.8%) was dripped onto the substrate 20 sec before the end. Finally, samples were annealed at 150 °C at least for 15 min in ambient air.

Rubrene:DBP film deposition and sample encapsulation

On top of these perovskite films the upconversion annihilator layer consisting of a rubrene (Sigma Aldrich, 99.99%):DBP (Sigma Aldrich, 98%) film was deposited by spin coating a 100µL solution at 6000 rpm for 20 sec with a ramp up of 3 sec. For this deposition, rubrene solution was prepared at a concentration of 10 mg/mL in anhydrous chlorobenzene and doped with DBP at a 1wt% ratio. These so-produced bilayer UC samples were then left uncovered in the glove box overnight to evaporate excess solvent. Finally, the samples were sealed with microscope glass cover slips using Blufixx epoxy and UV light under nitrogen. The film was shielded from the UV light pen during this process.

Film thickness, morphology and absorption measurements

Perovskite film thickness was determined using scanning electron microscope (SEM) images of cleaved sample cross-sections. The SEM system was from Zeiss Merlin (Gemeni 2) with a cold emission gun and in-lens secondary electron detection. A 5 kV accelerating voltage was used. Film thickness was measured at several points and averaged. The ITO/2PACz HTL substrate had an average perovskite film thickness of 170nm thick, and the glass substrate had an average perovskite film thickness of 180nm. SEM cross-sections are depicted in Figures S1B, S1D, S1F, and S1H. The rubrene layer thickness in both cases is approximately 50nm. A precise thickness determination from the SEM cross-section is difficult due to a lack of contrast in the image.

Film morphology was assessed from top view SEM images, as depicted in Figures S1A, S1C, S1E, and S1G. Films on both substrate types show a similar morphology, consisting of a mixture of predominantly large grains with >200nm length mixed with smaller grains that are clustered at the intersections of the larger grains. Addition of a rubrene layer adds a blurring effect to the SEM images, partially obscuring these details.

The absorption of the perovskite film prepared on both substrate types was recorded on a UV-vis-NIR spectrophotometer (Cary 5000). The decadic extinction was calculated using the film thickness values determined previously, and are plotted in Figure S2. The two film types exhibit near-identical extinction values, suggesting that the same perovskite material was generated regardless of the choice of substrate.

X-ray diffraction (XRD) diffractograms were obtained using a Bruker D8 diffractometer in Bragg-Brentano configuration at room temperature in air to compare the perovskite phase formation with respect to different substrates. The measurements were taken using the Cu K-alpha radiation emitted from an X-ray tube operated at an acceleration voltage of 40 kV and 40 mA. The diffractograms are shown in Figure S3. A sharp peak appeared at 13.9° in all four perovskite films, showing that the formation of the black α-phase was not disrupted by choice of substrate. The other sharp peak found at 28° corresponds to MA cation in the film, which is consistent with XRD reports for $FAMAPbI_3$.

Photoluminescence measurements

Photoluminescence (PL) measurements were carried out on a home-built confocal PL setup utilising a 90:10 transmission:reflection beamsplitter to separate the excitation and detection paths. Excitation was by a 700nm diode laser (IB-705-B laser head with Taiko driver, Picoquant) which could be operated in pulsed and cw modes. The laser beam was passed through a cleanup filter (FF01-700/13-25, Semrock) and the laser beam energy could be controlled by a computer-driven translation stage, which translated a linearly-gradiated neutral density filter through the beam path. During PL transient measurements, the laser was operated at a pulse repetition rate of 10kHz.

Focusing and PL collection was by an off-axis parabolic mirror with 5cm focal length, the laser spot was a circle with a 1/e diameter of approximately 35µm. Photoluminescence detection was by a silicon single-photon avalanche diode (Laser Components COUNT-50). The photoluminescence signal was selected by optical filters: a 715nm longpass filter (FF01-715/LP-25, Semrock) for the perovskite PL signal, and a pair of bandpass filters (HPX620-50 and HPM620-60, Newport Spectra-Physics GmbH) for the upconversion signal. The control software was a homebuilt Labview system.

For transient measurements, the PL count rate was recorded by TimeHarp260 Nano time-correlated single photon counting module (Picoquant). During cw measurements, the count rate was read out by a DAQ (NI). The count rate was adjusted with a motorised neutral density filter wheel when required.

The decay of carriers in the perovskite film was determined by recording transients of the perovskite PL for the ITO/2PACz/perovskite and ITO/2PACz/perovskite/rubrene samples, normalizing the transients to a peak height of 1.0, then taking the square root of the data. Taking the square root accounts for the fact that the PL transient represents the square of the film's carrier density due to the bimolecular nature of perovskite film photoluminescence. Carrier density transients derived from these are shown in Figure S6.

Surface photovoltage measurements

Transient SPV measurements were carried out a using femtosecond-pulsed 515 nm excitation laser at 10 kHz repetition rate. To better fill the large-area SPV electrode (6 mm diameter), the unfocused beam (1.8 mm 1/e diameter) was used. The beam had a Gaussian profile. The laser power was controlled with neutral density filters and monitored with a power meter. The highest-intensity transients, which are shown in Figure 2 of the main paper, were measured with a pulse energy density of 2.6 μJ/cm^2. The SPV signal was measured in the configuration of a parallel plate capacitor. The upper electrode comprised a quartz cylinder that also acts as a dielectric light guide, which is uniformly coated with SnO$_2$:F at the contact side and partially-coated on the cylinder barrel. The conductive coating is contacted with a gold ring that encompasses the cylinder and mechanically holds it. The cylinder pressed against the sample's encapsulation glass, which acted as an insulator. The lower electrode is the metal substrate of the SPV apparatus. SPV transients were read out using an oscilloscope, with 1000 averaged transients collected per measurement.

The choice of 515nm as the SPV excitation wavelength was made out of necessity, since excitation across the large-area electrode at 10 kHz required a laser system with substantial pulse energy, limiting us to using the second harmonic of the 1030 nm fundamental of an amplified fiber oscillator femtosecond laser. In tests using a separate lower-repetition rate laser, we found that the SPV transient dynamics were unchanged when 515nm and 700nm excitation wavelengths were used.

Optical excitation during SPV measurements was through the annihilator layer, to best match the conditions of the PL measurements. Although a small amount of pump light absorption in the rubrene layer took place using this configuration, this did not generate any SPV signal and is negligible. Further, SPV transients measured with excitation delivered through the perovskite and the rubrene layers did not show any appreciable differences.

Surface photovoltage transient modelling

Equations 2, 3, 4, 5, 6, 7, 8, and 9 (below) and Figure S4 describe the phenomenological model for charge separation, trapping, detrapping, and recombination, used to computationally simulate the measured SPV transients. n and p refer to the concentration of photo-induced electrons and holes. n_{SAM} and p_{SAM} are the concentration of extracted electrons and holes to ITO/SAM interface (SAM refers to the 2PACz self-assembled monolayer on ITO). n_R and p_R are the concentration of extracted electrons and holes in the rubrene interface. The difference in holes and electron concentration in the ITO/SAM, perovskite, and rubrene layers induces the SPV signal, as shown by Equation 9.

The constants K_e and K_h correspond to the electron and hole injection rate constants from perovskite to the system comprised of the ITO/SAM. The constants $\tilde{K}_h$ and $\tilde{K}_e$ correspond to hole and electron injection rates from perovskite to rubrene. Similarly, K_{eb} and K_{hb} are reinjection rates of electron and hole to perovskite from ITO/SAM, which effectively includes back tunneling/thermionic emission, diffusion of the free carriers, and the drift of the free carriers due to the presence of the space charge. $\tilde{K}_{eb}$ and $\tilde{K}_{hb}$ are reinjection rate constants of electron and hole to perovskite from rubrene. C_b is the perovskite radiative recombination constant. N_t and σ are concentration and capture cross-sections of defects responsible for SRH non-radiative recombination. N_{St} and σ_S are concentration and capture cross-section of surface defect. τ_R characterizes the effective carriers' lifetime in rubrene. τ_D is the surface trap retention lifetime. The system of the equations cannot be solved analytically; therefore, we used the Adams backward differentiation formula (BDF) solving algorithm. We used the Levenberg-Marquardt method to fit constants in order to minimise deviation from the experimental SPV results. Measured SPV data were extrapolated logarithmically for quicker optimization of fitting. The modelled transients resulting from the fit are given in main text Figure 2, and the fit parameters are in Tables S1 and S2.

$$\frac{dp}{dt} = -K_h p + K_{hb} p_{ITO} - \tilde{K}_h p + \tilde{K_{hb}} p_R - C_b(pn) - p\sigma_{ht}v_h n_t - p\sigma_{Sh}v_h n_{St} \qquad \text{(Equation 2)}$$

$$\frac{dn}{dt} = -K_e n + K_{eb} n_{ITO} - \tilde{K}_e n + \tilde{K_{eb}} n_R - C_b(np) - n\sigma_{et}v_e(N_t - n_t) - n\sigma_{Se}v_e(N_{St} - n_{St}) + \frac{n_{St}}{\tau_D}$$
$$\text{(Equation 3)}$$

$$\frac{dp_{ITO}}{dt} = K_h p - K_{hb} p_{ITO} \qquad \text{(Equation 4)}$$

$$\frac{dn_{ITO}}{dt} = K_e n - K_{eb} n_{ITO} \qquad \text{(Equation 5)}$$

$$\frac{dp_R}{dt} = -\tilde{K}_h p + \tilde{K_{hb}} p_R - \frac{p_R}{\tau_R} \qquad \text{(Equation 6)}$$

$$\frac{dn_R}{dt} = -\tilde{K}_e n + \tilde{K_{eb}} n_R - \frac{n_R}{\tau_R} \qquad \text{(Equation 7)}$$

$$\frac{dn_t}{dt} = n\sigma_e v_e(N_t - n_t) - p\sigma_h v_h n_t \qquad \text{(Equation 8)}$$

$$\frac{dn_{St}}{dt} = n\sigma_{Se}v_e(N_{St} - n_{St}) - p\sigma_{Sh}v_h n_{St} - n_{St}/\tau_D \qquad \text{(Equation 9)}$$

We assume a uniform distribution of charges inside each of the device layers, such that the total charge density can be represented at a single point. The SPV signal can hence be simplified to yield the following: (given as Equation 1 in the main text).

$$SPV = \left(L_1 \frac{p_R - n_R}{\varepsilon_R} + L_2 \frac{n_{ITO} - p_{ITO}}{\varepsilon_{ITO}} + L_3 \frac{p_P - n_P - n_t}{\varepsilon_P} + L_3 \frac{n_{St}}{\varepsilon_P} \right) \times \frac{d_P}{2\varepsilon_0}$$

where $L_1 = (d_P + d_R)/2$, $L_2 = (d_P + d_{ITO})/2$, and $L_3 = d_P/2$, representing charge separation distances, and d_P is the thicknesses of perovskite layer. d_{HTL} and d_R represent the mean depths from the interface at which free carriers reside in the ITO and rubrene layers (10 nm and 30 nm respectively). d_{ITO} and d_R act as a kind of weighted spatial average representing the actual charge distribution in a real sample. Due to the quasi-metallic nature of ITO, we assume that charging of the layer manifests as charges residing near to the interface. The calculation of SPV in Equation 9 uses surface charge density, which we obtain using the factor of d_P.

The values of several interface-specific fit constants change when the device structure does, according to the fit-optimized values obtained. Enforcing fit conditions that applied a constant set of values in different devices, we were unable to obtain good fit solutions. We rationalise this as a result of our fitting model being phenomenological, wherein several physical processes are compressed into one rate. Altered energy level alignments, defect densities and sample charging that result from changes in the device structure (e.g. from addition of a second p-layer) can therefore result in changes to various rate constants associated with charge transfer at a certain interface.

To retain maximum generality and the concept of interface selectivity in the model, we did not enforce any carrier-selective properties for any particular interface and let the fit optimization arrive at the values shown. The results therefore show some accumulation of electrons in the notionally hole-selective rubrene and ITO/2PACz layers, although overall the rubrene and ITO/SAM interfaces in the model did display a pronounced preference for hole extraction, in line with their function in real devices. We assumed that electrons and holes co-located in a given transport layer corresponded with recombination, with electrons cancelling the SPV contribution of an equal quantity of holes in the same layer. The carrier density transients shown in Figure 2 are, correspondingly, calculated as the difference between the layer's simulated hole and electron density transients, whereas the figures in section S5 show the direct simulation output. We forced the ITO/2PACz hole density transient to zero when the electron density rose higher than the hole density, which occurred only towards the end stages of the transient, rather than allowing the hole density to

become negative. This non-physical situation likely arises due to the lack of enforced carrier selectivity in our model, and it does not affect our findings in any way.

Steady-state carrier density calculation

The photoexcited carrier density for a neat perovskite film under continuous wave illumination was estimated using the following simple rate model:

$$\frac{dn}{dt} = G - nk_{SRH} - Bn^2$$

where n is the density of photoexcited electrons (we assume $n = p$, where p is the photoexcited hole density), G is the carrier generation rate, k_{SRH} is the reciprocal of the Shockley-Read-Hall lifetime, and B is the radiative recombination rate constant. Assuming steady state conditions such that $\frac{dn}{dt} = 0$, a solution is as follows:

$$n = \frac{-k_{SRH} + \sqrt{k_{SRH}^2 + 4BG}}{2B} \qquad \text{(Equation 10)}$$

G was calculated by considering the excitation density, spot size and sample absorption. Values are given in Table S3.